



# Boron-doping on the surface mediated low-valence Co centers in cobalt phosphide for improved electrocatalytic hydrogen evolution

Yingying Gao<sup>a,1</sup>, Sheng Qian<sup>a,1</sup>, Haijiao Wang<sup>c</sup>, Wenzhi Yuan<sup>a</sup>, Yu Fan<sup>a</sup>, Ningyan Cheng<sup>b,\*</sup>, Huaiguo Xue<sup>a</sup>, Tengfei Jiang<sup>a,\*</sup>, Jingqi Tian<sup>a,\*</sup>

<sup>a</sup> School of Chemistry and Chemical Engineering, and Institute for Innovative Materials and Energy, Yangzhou University, 180 Si-Wang-Ting Road, Yangzhou 225002, PR China

<sup>b</sup> Information Materials and Intelligent Sensing Laboratory of Anhui Province, Key Laboratory of Structure and Functional Regulation of Hybrid Materials of Ministry of Education, Institutes of Physical Science and Information Technology, Anhui University, Hefei 230601, PR China

<sup>c</sup> Electric Power Research Institute of State Grid Heilongjiang Electric Power Company Limited, 7 Xiang-jiang Road, Harbin 150001, PR China

## ARTICLE INFO

### Keywords:

Electrochemical hydrogen evolution reaction  
Surface-confined doping  
Electronic structure  
Transition metal phosphide  
Low-valence metal centers

## ABSTRACT

Rationally engineering the surface structure of transition metal phosphides (TMPs) could regulate valence state of metal centers ( $M^{\delta+}$ ) with optimized binding strength of  $H_2O$  and  $H^*$  and relative Gibbs free energy ( $\Delta G_{H^*}$ ) in alkaline hydrogen evolution reaction (HER). However, the precise location of such metal centers is still challenging due to the limited synthetic methodology. Herein we report the surface-layer-confined doping of boron on cobalt phosphide nanowire arrays (B-CoP) via a controllable surface redox reaction. Nanowire CoP decorated with B-doped surface layer structure has proved to be an outstanding HER electrocatalyst, with an overpotential of 112 mV at 100  $mA\ cm^{-2}$ . X-ray absorption near edge structure (XANES) and X-ray photoelectron spectroscopy (XPS) analysis, and theoretical results demonstrate that B-doping induced electron redistribution of Co with electron-rich features. Such low-valence Co centers coordinated with B can achieve strong affinity toward  $H_2O$  molecules and optimized  $\Delta G_{H^*}$  to accelerating reaction kinetics.

## 1. Introduction

The ever-increasing consumption of exhaustible fossils with carbon dioxide emission causes the exploration of renewable and clean energy resources [1]. With high energy density and zero-carbon content, hydrogen has been considered as one of the most promising green and sustainable energy carrier for clean fuel [2]. Electrochemical water splitting has attracted significant attention as a key pathway for large scale hydrogen production [3]. Hydrogen evolution reaction (HER) occurs on the cathode, is an uphill reaction which requires large overpotential as the main barriers for water electrolysis [4]. Therefore, the development of HER catalyst is necessary to reduce the overpotential and accelerate the reaction dynamics. Currently, Pt-based electrocatalysts exhibit the most effective activities for HER, but their large-scale application is inhibited by the scarcity and high cost [5]. Therefore, the exploitation of highly-efficient non-precious alternatives is critical but still facing great challenge. Transition metal phosphides (TMPs) have attracted extensive research interest as HER catalysts

owing to their advantages in electrical conductivity, mechanical strength and chemical and thermal stability [7,8]. Pioneering works demonstrated that the negatively charged phosphorus atom in TMPs favors the adsorption of active H species to form  $P-H_{ad}$  intermediate due to their electronegativity, but such strong-binding would lead to unfavorable Gibbs free energy for hydrogen adsorption ( $\Delta G_{H^*}$ ), hampering the desorption and combination for  $H_2$  release in Tafel and/or Heyrovsky step [9–11]. To this end, regulating the binding strength of  $P-H_{ad}$  and the relative  $\Delta G_{H^*}$  would be beneficial to TMPs with improved HER activities.

Tremendous research efforts have been devoted to engineering the  $\Delta G_{H^*}$ , a commonly accepted descriptor in TMP-catalyzed HER [12–16]. Guidelines are offered for judiciously engineering the electronic structure of TMPs to boost the intrinsic activities of HER, mainly through heteroatom doping, defect construction, and crystal/amorphous conversion. The incorporation of heteroatom with varied electronegativities into TMPs has been confirmed as a powerful strategy to create new active sites, redistributing the electron densities and optimize the

\* Corresponding authors.

E-mail addresses: [ningyancheng@ahu.edu.cn](mailto:ningyancheng@ahu.edu.cn) (N. Cheng), [jiangtengfei@yzu.edu.cn](mailto:jiangtengfei@yzu.edu.cn) (T. Jiang), [tianjq@yzu.edu.cn](mailto:tianjq@yzu.edu.cn) (J. Tian).

<sup>1</sup> These authors contribute equally to this work.

formation energy of intermediates toward a boosted HER performance [17–22]. In general, the nonmetal doping atoms such as O, S, N, and Se are commonly used owing to their larger electronegativity compared with that of P, enabling distorted electron density and easily form high-valence metal centers in TMPs. For a specialized catalytic reaction such as HER, the valence-state of metal state could be regulated in another direction, that is, through doping the relative lower electronegativity B into TMPs to form low-valence metal centers. For instance, Cao et al. reported the bulk-doping of B in CoP induced electronic structure reformation of CoP with low-valence Co centers, which afforded improved pH-universal HER performance [23]. Such demonstration provides opportunities for the design of B-doped TMPs with desired electron structure regulation.

Inspired by the aforementioned design rationales, we proposed a feasible strategy to fabricate surface-layer-confined doping of boron on self-supported cobalt phosphide nanowire arrays (B-CoP) via a controllable surface redox reaction. The Co centers coordinated with B in the surface layer are more active for HER compared with these in undoped CoP. Both experimental results and the density functional theory (DFT) calculations reveal that B-doping induced electron redistribution and altered d-band structure of Co to form low-valence Co centers, resulting in optimized  $\Delta G_{H^+}$  and accelerated reaction kinetics. Such B-CoP exhibits remarkably-enhanced HER performance with a overpotential of 112 mV at the current density of 100 mA cm<sup>-2</sup> compared with that (169 mV) of undoped CoP.

## 2. Experimental

### 2.1. Materials

All the reagents used in this study were of analytical grade and used without further purification. Co(NO<sub>3</sub>)<sub>2</sub>·0.6 H<sub>2</sub>O, NaH<sub>2</sub>PO<sub>2</sub> were purchased from Sigma-Aldrich Pte. Ltd. (Singapore). NaBH<sub>4</sub>, NH<sub>4</sub>F, CO (NH<sub>2</sub>)<sub>2</sub>, KOH and HCl was provided by Sinopharm Chemical Reagent Co. Ltd. Titanium mesh with 0.35 mm in wire diameter was purchased from Wintek Technology Pte. Ltd. The water used throughout all experiments was purified using a Millipore system.

### 2.2. Fabrication of Co(OH)F nanowire arrays (Co(OH)F)

The Co(OH)F nanowire arrays were prepared immersing a piece of Ti mesh (2 cm × 3 cm) pretreated by HCl (6 M) into a aqueous solution (20 mL) of Co(NO<sub>3</sub>)<sub>2</sub>·0.6 H<sub>2</sub>O (2 mmol), CO(NH<sub>2</sub>)<sub>2</sub> (50 mmol) and NH<sub>4</sub>F (2 mmol). The hydrothermal reaction was conducted in a sealed autoclave at 120 °C for 6 h. After cooling down to room temperature, the obtained product was taken out and thoroughly rinsed with deionized water before drying.

### 2.3. Surface redox reaction for the fabrication of boron-doped Co(OH)F nanorod arrays (B-Co(OH)F)

Typically, a piece of Co(OH)F (2 cm × 3 cm) was immersed into NaBH<sub>4</sub> aqueous solution (10 wt%) at room temperature to accomplish the surface redox reaction. Then the product was rinsed repeatedly to remove the adsorbed ions. Varying the period of redox reaction led to different thickness of the surface layer.

### 2.4. Fabrication of surface layer-confined-doping of boron on CoP (B-CoP)

The prepared B-Co(OH)F was converted into B-CoP via phosphidation. Typically, B-Co(OH)F and NaH<sub>2</sub>PO<sub>2</sub> were placed in the tube furnace and annealed at 320 °C for 2 h at a ramp rate of 1 °C min<sup>-1</sup> in argon. As a control sample, pristine CoP without B-doping at the surface was also fabricated in a similar way in the absence of the surface redox reaction with NaBH<sub>4</sub>. Such prepared B-CoP electrode with an average

mass loading of ca. 1.5 mg cm<sup>-2</sup>.

### 2.5. Materials characterization

X-ray diffraction (XRD) analysis was conducted on a Bruker D8 Advance with Cu K $\alpha$  radiation ( $\lambda = 1.5406 \text{ \AA}$ ). The morphology of the samples were characterized by a field-emission scanning electron microscopy (FESEM, Zeiss Supra55), and transmission electron microscopy (TEM, Tecnai G2 F30 S-TWIN operated at 300 kV) and a scanning transmission electron microscope (STEM, JEOL JEM-ARM200 f). X-ray photoelectron spectroscopy (XPS) measurements were performed using an ESCALAB 250Xi using Mg as the excitation source with C 1 s (284.6 eV) calibration. X-ray absorption near-edge structure (XANES) were measured at the BL14W1 beamline of Singapore Synchrotron Radiation Facility.

### 2.6. Electrochemical HER tests

The electrochemical tests were performed on a CHI 660D electrochemical workstation (CH Instruments) with a standard three-electrode cell. The prepared B-CoP was directly used as the working electrode (0.25 cm<sup>2</sup>), while a saturated calomel electrode (SCE) and a graphite plate were used as the reference and counter electrode, respectively. The linear sweep voltammetry (LSV) curves were collected at a scan rate of 2 mV s<sup>-1</sup>. Chronopotentiometric measurements were recorded by applying a current density of 100 mA cm<sup>-2</sup>. Electrochemical impedance spectroscopy (EIS) was recorded in the frequency range of 0.1–100 kHz. Potentials were referenced to a reversible hydrogen electrode (RHE) according to Eq. (1).

$$E_{RHE} = E_{SCE} + 0.059 \times pH + 0.242 \quad (1)$$

All electrochemical data was shown with *iR* correction.

### 2.7. Computational methods

All calculations were performed in the code of Vienna Ab initio Simulation Package (VASP) [24] with the projector augmented wave (PAW) method [25]. The exchange-functional is treated using the generalized gradient approximation (GGA) of Perdew-Burke-Ernzerhof (PBE) [24] functional. The cut-off energy of the plane-wave basis is set at 450 eV for optimize calculations of atoms and cell optimization. The vacuum spacing in a direction perpendicular to the plane of the catalyst is at least 15 Å. The Brillouin zone integration is performed using 3 × 3 × 1 Monkhorst-Pack k-point sampling for a primitive cell [26]. The self-consistent calculations apply a convergence energy threshold of 10<sup>-5</sup> eV. The equilibrium lattice constants are optimized with maximum stress on each atom within 0.05 eV/Å. The Hubbard U (DFT+U) corrections for 3d transition metal by setting according to the literature [27].

The free energy was calculated according to Eq. (2) [28].

$$G = E + ZPE - TS \quad (2)$$

Where *G*, *E*, *ZPE* and *TS* are the free energy, total energy from DFT calculations, zero point energy and entropic contributions (*T* was set to be 300 K), respectively. *ZPE* could be derived after frequency calculation according to Eq. (3) [29].

$$ZPE = \frac{1}{2} \sum \hbar \nu_i \quad (3)$$

And the *TS* values of adsorbed species are calculated after obtaining the vibrational frequencies according to Eq. (4) [30].

$$TS_{\nu} = k_B T \left[ \sum_K \ln \left( \frac{1}{1 - e^{-\hbar \nu / k_B T}} \right) + \sum_K \frac{\hbar \nu}{k_B T} \left( \frac{1}{e^{\hbar \nu / k_B T} - 1} \right) + 1 \right] \quad (4)$$

### 3. Results and discussion

#### 3.1. Synthesis and structure characterization of B-CoP

The preparation process of surface confined-doping of boron on cobalt phosphide nanowire arrays (B-CoP) is illustrated in Fig. 1a, which involves the sequent hydrothermal growth of Co(OH)F, redox reaction between Co(OH)F with NaBH<sub>4</sub> to implant element boron into the surface layer of Co(OH)F, and phosphidation to convert the precursor into phosphide with surface-layer-confined doping of boron. The XRD patterns reveal that Co(OH)F precursor and B-Co(OH)F exhibit the same diffraction peaks (JCPDS No. 50–0827) [31], as shown in Fig. S1, indicating the surface-redox reaction has little influence on the crystal structure of Co(OH)F precursor. Accordingly, the diffraction peaks for both pristine CoP and B-CoP in Fig. 1b could be correspond to CoP (JCPDS No. 29–0497) [32], which suggests that B-CoP and CoP share the same crystal structure. To track the morphology evolution of the materials, scanning electron microscopy (SEM) and transition electron microscopy (TEM) image were shown in Figs. 1c and 1d, revealing that such B-CoP are nanowire arrays with diameters of 100–200 nm and

length of several micrometers. High-resolution TEM (HRTEM) image further shows there is an amorphous layer with ca. 6.5 nm in thickness decorated on the crystal core, leading to enlarged diameter of B-CoP nanowire compared with that of pristine CoP (Fig. S2). This could be attributed to the implantation of B into the lattice of CoP induced amorphization of the surface layer, which results in swelling of the lattice with disordered atom arrangement. HRTEM in Fig. 1e shows that the spacing of 0.247 nm and 0.163 nm was attributed to the (111) and (212) facet of CoP, respectively. An enlarged HRTEM image taken from the surface layer has been provided. There is no obvious crystal domains in the layer, which presents amorphous nature. The selected area electron diffraction (SAED) suggested that the major diffraction rings indexed to (111), (200), (002) and (210) planes of CoP [33], which is matched well with the XRD result of B-CoP (Fig. 1f). The HAADF-STEM elemental mapping of B-CoP further confirmed Co and P elements were both homogeneously distributed throughout the entire area of the nanowire, while the signal of B tends to be more concentrated on the edge than in the core on the nanowire (Fig. 1g). The formation of such amorphous layer on CoP was realized via a surface redox reaction followed by phosphidation. In the redox reaction between Co(OH)F with aqueous

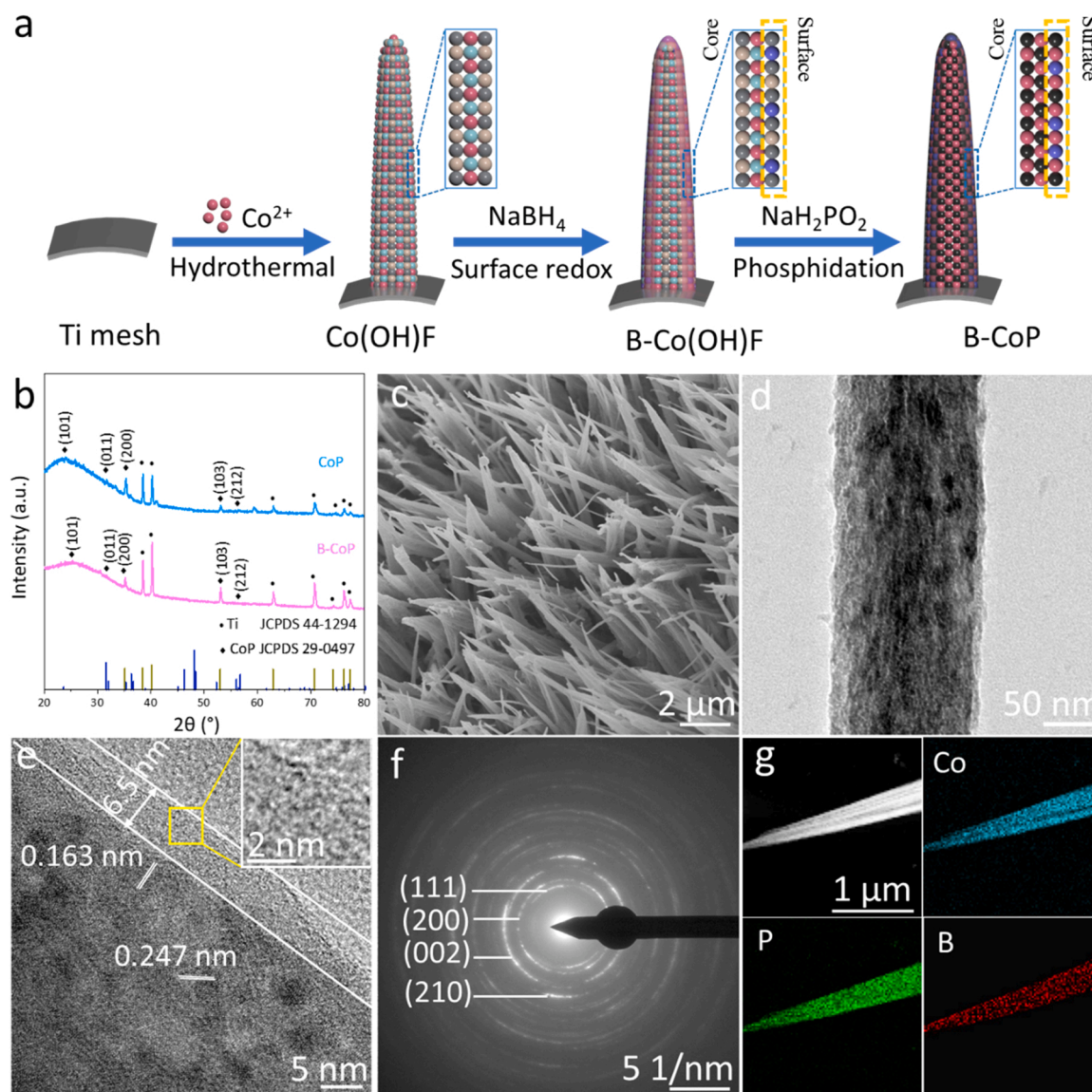


**Fig. 1.** (a) Synthesis procedure of B-CoP; (b) XRD patterns of CoP and B-CoP; (c) SEM image and (d) TEM image of B-CoP; (e) HRTEM image taken from the surface from one B-CoP nanowire. Inset: enlarged image of the marked area; (f) SAED patterns taken from the surface from one B-CoP nanowire; (g) STEM and element mapping images of B-CoP.



solution of  $\text{NaBH}_4$ ,  $\text{CoB}_x$  could be formed on the surface of nanowire, in which Co possesses low valence state below +2 owing to the strong reduction ability of  $\text{NaBH}_4$ . During the following phosphidation, such  $\text{CoB}_x$  could be preserved owing to the low-valence Co in  $\text{CoB}_x$  compared with that in CoP, leading to B-doped CoP on the surface layer. As comparison, B-CoP nanowire with varied thickness of surface-doping layer have been fabricated (Fig. S3). The thickness of the surface layer could be regulated in the range of  $\sim 2\text{--}10\text{ nm}$ . The content of B on the B-CoP was evaluated by the energy dispersive spectroscopy (EDS) to be 1.89%, 3.01%, and 4.68% for B-CoP-1 min, B-CoP-5 min, and B-CoP-10 min, respectively (Fig. S4).

### 3.2. Electronic structure analysis of B-CoP

The surface chemistry of B-CoP and CoP were investigated by X-ray photoelectron spectroscopy (XPS). The XPS survey spectrum discloses the presence of Co, P, O and B in B-CoP (Fig. S5). In Co 2p spectrum of B-CoP (Fig. 2a), the peaks located at 779.1 eV and 794.1 eV could be identified as  $\text{Co}^{\delta+}$  in CoP, and the peaks located at 782.1 eV and 798.3 eV were ascribed to oxidized Co species [32,33]. The coincidence of Co-P and Co-B located at 779.1 eV and 794.1 eV could be recognized in the Co 2p spectrum. In the P 2p spectrum of B-CoP (Fig. 2b), there are two peaks located at 130.2 eV and 129.3 eV corresponding to  $\text{P}^{\delta-}$  in CoP, while the peak at 134.3 eV could be attributed to  $\text{PO}_x$  due to the surface oxidation of CoP in the air [34]. Compared with pristine CoP, it is observed that surface-doping of B induces a negative shift of 0.6 eV in Co 2p and 0.3 eV in P 2p, respectively. These shifts in XPS spectra could be ascribed the fact that B possesses lower electronegativity compared with P, which results in the weaker capacity of electron-withdraw, leading to higher electron density around the coordinated Co atoms. Meanwhile, B can also regulate the electron density of the adjacent P upon the coordinated Co, where the Co atoms with enhanced electron-donating ability could induce more electrons occupy in P 2p to form electron-rich P atom [11]. Meanwhile, the B 1s XPS spectrum of the B-CoP (Fig. 2c) exhibits the Co-B peak at 187.4 eV and B-O peak at 191.8 eV, respectively [23, 35]. Combining with distinguished B-Co peak in the B 1s spectrum, the

formation of Co-B bond is strongly evidenced. All the above results indicate the B-doping induced the electron-redistribution on the surface layer of B-CoP, which leads the formation of electron-rich Co and P centers in CoP, holding great promise for efficient electrocatalytic HER.

The coordination structure of Co centers in B-CoP were further illustrated by the X-ray absorption fine structure (XAFS). The Co K-edge X-ray absorption near-edge structure (XANES) and Fourier transform extended X-ray absorption fine structure (FT-EXAFS) spectra of CoP, B-CoP, CoO and Co foil are shown in Figs. 2d and 2e. It can be seen that the Co K-edge position of B-CoP and CoP is located between those Co foil and CoO, indicating the oxidation state of Co between 0 and +2 for both samples. Impressively, B-CoP exhibits a further lower Co-edge position compared with that of CoP, suggesting increased average electron densities around the Co sites in B-CoP, which is consistent with the XPS analysis. Based on the Fourier transform (FT)  $k^3$ -weighted extended X-ray absorption fine structure (FT-EXAFS) spectra of the Co K-edge (Fig. 2e), there is one dominant peak at  $1.65\text{ \AA}$  in B-CoP, attributed to Co-P bond [36,37]. Other peaks located at 1.68, 2.18 and  $2.61\text{ \AA}$  were assigned to the bond of Co-O, Co-Co respectively. As expected, the Co-P peak exhibits a slight shift from  $1.68\text{ \AA}$  to  $1.65\text{ \AA}$  in B-CoP and CoP along with decreased intensity, which is probably caused by the formation of shorter Co-B bond length. Such shorter Co-B bond evidences the strengthened interaction between Co and B, which might facilitate charge transfer in the electrocatalytic processes. The wavelet transforms (WT) of Co K-edge EXAFS oscillations of B-CoP shows a maximum value at  $4.8\text{ \AA}^{-1}$ , also assigned to the Co-P bond, which shifts to the lower value compared with that of CoP ( $5.1\text{ \AA}^{-1}$ , Fig. 2f). The EXAFS fitting was performed to extract the structure parameters of Co centers (Fig. S6 and Table S1).

### 3.3. Electrocatalytic performance of alkaline HER

To explore the HER activity of B-CoP, the electrochemical tests were conducted in a traditional three-electrode cell with 1.0 M KOH as electrolyte. As the linear sweep voltammetry (LSV) curves shown in Fig. 3a, B-CoP outperforms pristine CoP throughout the entire HER test, only

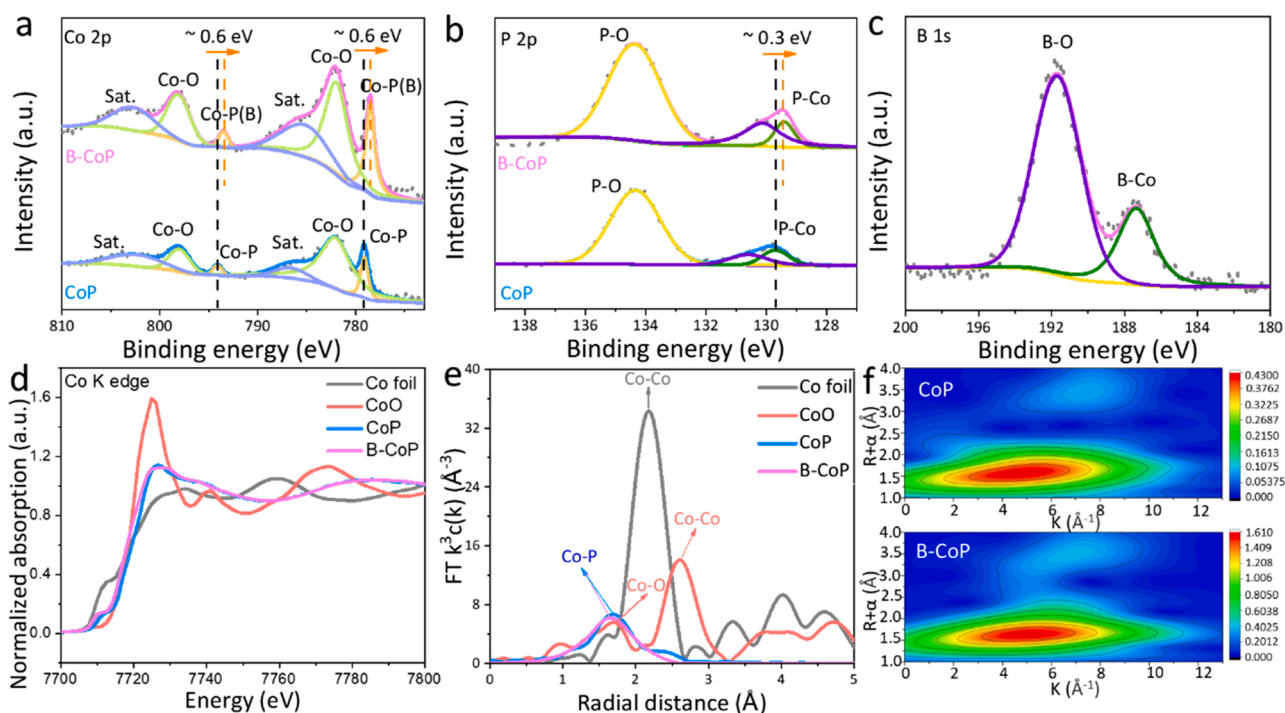


**Fig. 2.** High-resolution XPS spectra of (a) Co 2p, (b) P 2p, (c) B 1s in B-CoP and CoP; (d) Co K-edge XANES spectra of B-CoP, CoP, Co foil and CoO; (e) the corresponding FT EXAFS spectra; (f) the corresponding Wavelet Transform (WT) contour plots of the EXAFS signals of CoP and B-CoP.

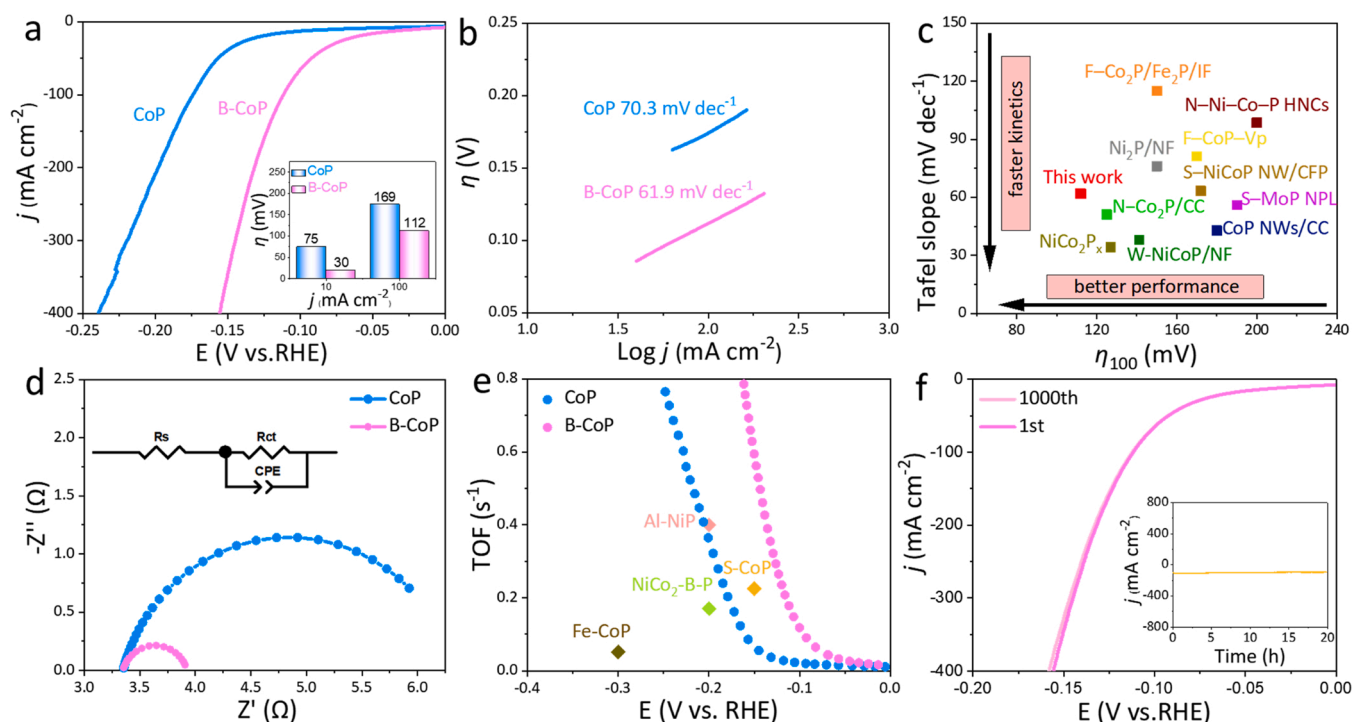


**Fig. 3.** (a) LSV curves of B-CoP and CoP in 1.0 M KOH at a scan rate of 2 mV s<sup>-1</sup>. Inset: comparison of overpotentials at different current densities for corresponding electrodes; (b) Tafel slopes; (c) Comparison of the HER performance of the B-CoP with other advanced electrocatalysts; (d) Nyquist plots of corresponding electrodes; (e) TOF values of B-CoP, CoP, and some recently reported HER electrocatalysts; (f) LSV curves of B-CoP before and after 1000 cycles. Inset: chronopotentiometry test during a period of 20 h.

requires an overpotential of 112 mV to achieve HER current density of 100 mA cm<sup>-2</sup>, which is notably smaller than that of CoP (η<sub>100</sub> = 169 mV). Tafel slopes were calculated from the polarization curves to evaluate the reaction kinetics. B-CoP shows a smaller Tafel slope compared with that of CoP (61.9 mV dec<sup>-1</sup> vs 70.3 mV dec<sup>-1</sup>) (Fig. 3b), indicating a Volmer-Heyrovsky mechanism-based HER. The low and Tafel slope endow B-CoP among the best TMP-based electrocatalysts for alkaline HER (Fig. 3c and Table S2). EIS measurements were carried out to further investigate the electrode kinetics of HER (Fig. 3d). The semicircles in the high- and low-frequency range of the Nyquist plot could be ascribed to the charge-transfer resistance (R<sub>CT</sub>) and solution resistance (R<sub>s</sub>), respectively. Specially, B-CoP exhibits smaller R<sub>CT</sub> of 0.58 Ω compared with that of CoP (2.98 Ω), suggesting enhanced charge transport kinetics induced by surface-confined B-doping [38].

To further investigate the influence of B-doping on the HER performance of CoP, B-CoP with varied content of B-dopant in term of different thickness of surface layers have been applied as control samples for HER. It is found the η<sub>100</sub> of B-CoP samples present a volcano profile as a function of the surface-redox period (Fig. S7c), in which B-CoP-5 min exhibits the highest HER activity. Both the amount of surface active sites and charge transfer resistance are critical to electrocatalytic performance. A short surface redox period cannot provide enough B-coordinated Co sites for HER, while a too long surface redox period led to a thicker surface layer, which is more obstructive for charge transfer between the surface and conductive core, therefore depressing HER performance.

It is believed the electrocatalytic performance is also affected by the electrochemical surface area (ECSA), thus the electrical double-layer capacitances (C<sub>dl</sub>) measurements of different samples were used to determine ECSA. As shown in Fig. S8, the ECSA of B-CoP and CoP is calculated to be 62.1 cm<sup>2</sup> mg<sup>-1</sup> and 59.2 cm<sup>2</sup> mg<sup>-1</sup>, respectively. The facilitated charge transfer and increased ECSA for B-CoP could be attributed to surface-confined B-doping induced amorphization with disordered atomic arrangement creates abundant active centers on the

surface, while retains the conductivity of the inner phosphide. Moreover, we also evaluated the turnover frequency (TOF) of B-CoP and CoP in Fig. 3e. At an overpotential of 150 mV, the TOF of B-CoP and CoP is 0.59 s<sup>-1</sup> and 0.06 s<sup>-1</sup>, respectively, which validates that B-CoP has higher intrinsic activity, demonstrating surface-confined B-doping can significantly enhance the per-site activity for HER.

The long-term stability of B-CoP was enumerated in Fig. 3f. After 1000 cycles, the HER activity exhibits negligible change. Additionally, B-CoP electrode maintains 98% of the initial current density of 100 mA cm<sup>-2</sup> after 20 h continuous electrolysis, similar to pristine CoP (Fig. S9), indicating the excellent stability of B-CoP for HER.

### 3.4. DFT calculation

Density functional theory (DFT) calculations were performed to further clarify the mechanism of surface-B-doping for boosted HER performance. The calculation model were established based on CoP (101), and a surface P atom replaced by B and coordinated with adjacent Co for B-CoP (101) (Fig. 4a). As shown in Fig. 4b, the Bader charge analysis is used to determine the charge transfer quantitatively. In pristine CoP, Co loses ca. 0.31 electrons to P. Upon B substitution, the neighboring Co loses less electrons (0.25), leading to electron accumulation at Co centers, which favors decreasing the energy barrier of H<sub>2</sub>O dissociation [20]. Considering that the adsorption of H<sub>2</sub>O molecule on the catalyst surface is a crucial step in HER kinetics, the interaction between H<sub>2</sub>O and catalyst surface was investigated. B-CoP give a more negative adsorption energy (E<sub>H2O</sub>) than CoP, which confirms the stronger adsorption of H<sub>2</sub>O on B-CoP (Fig. 4c). Such favorable adsorption of H<sub>2</sub>O promotes the kinetics of Volmer step. The wettability test confirms the better water affinity of B-CoP compared with CoP, as shown in Fig. S11. The water droplet spreads more rapidly on B-CoP, revealing the hydrophilicity rendered by B-doping. The Gibbs free energy of H adsorption (ΔG<sub>H\*</sub>) is regarded as an important descriptor in HER, which should be thermo-neutral with balanced adsorption and desorption of H

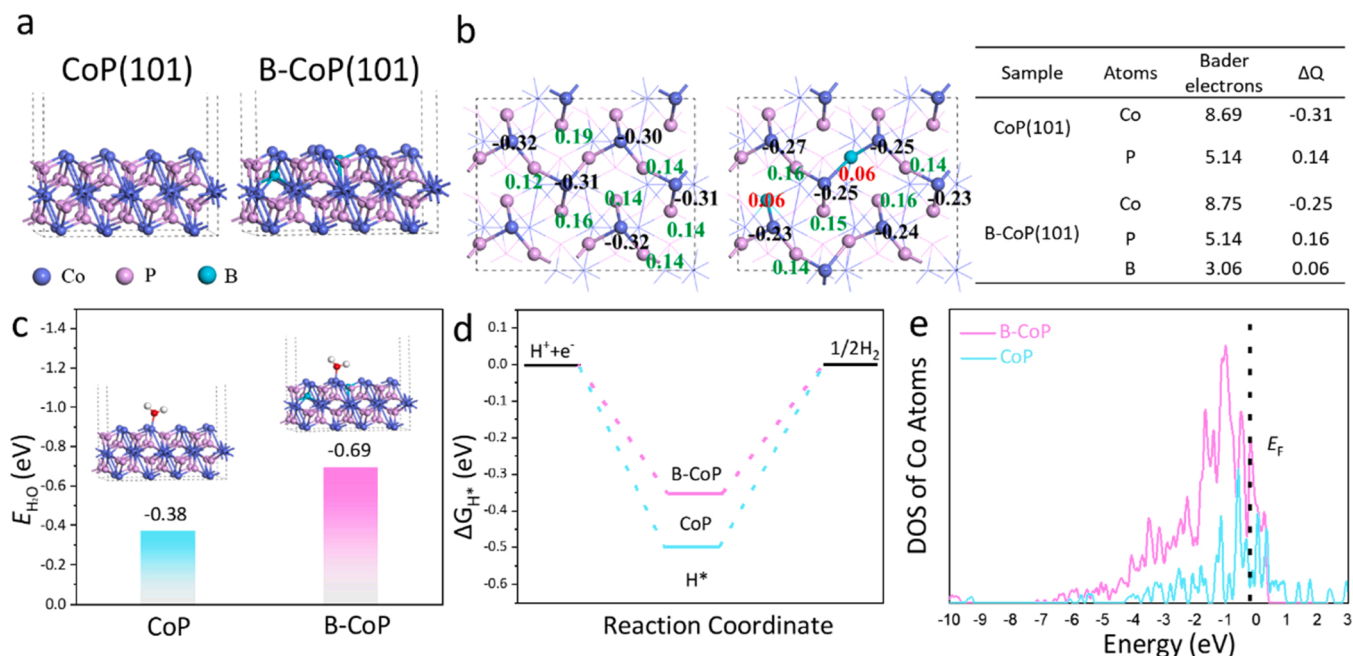


**Fig. 4.** (a) Optimized models for hydrogen adsorption at the Co-Co bridge site of pristine CoP (101) surface and CoP (101) with B doping; (b) Bader charge of surface atoms of CoP and B-CoP; (c) Molecular adsorption of water on the Co site of CoP and B-CoP; (d) Free-energy diagram for HER; (e) Calculated DOS of surface Co atoms d orbitals on the pristine CoP (101) and CoP (101) surface with B doping.

for an optimal catalyst [39]. As shown in Fig. 4d, the  $\Delta G_{H^*}$  for B-CoP is calculated to be  $-0.69$  eV, which is more close to zero than that of CoP ( $-0.38$  eV), suggesting a relatively weak adsorption of H atoms and promoted HER. Fig. 4e presents the calculated *d*-orbital partial density of states (PDOS) of Co in B-CoP and CoP, demonstrating the lower-lying *d*-band center of B-CoP than CoP. According to the *d*-band theory, a lower-lying *d*-band center leads to weakened adsorption of H on the catalysts surface [40]. Meanwhile, B-CoP presents a high state in the low DOS region close to Fermi level, demonstrating high conductivity and fast electron transfer during electrocatalysis [27]. Taken together, the experimental and theoretical results confirm that surface-confined B-doping induced electron redistribution for engineering the electronic structure of CoP, leading to optimized  $\Delta G_{H^*}$  and accelerated reaction kinetics.

### 3.5. Post-analysis after long-term electrolysis

To further investigate the morphological and electronic structure of B-CoP after long-term electrolysis, systematic characterizations including SEM, TEM, XRD and XPS analyses were performed on the post-electrocatalyst (Fig. 5). After 20 h-continuous electrolysis at a static potential of 1.39 V vs. RHE, B-CoP maintains its nanowire structure as revealed by SEM and TEM (Figs. 5a, 5b). The HRTEM image shows the formation of several small nanoparticles with average size of ca. 3 nm in the amorphous surface layer, with characteristic fringe spacing of 0.213 and 0.246 nm which could be indexed to the (111) and (200) facet of CoO, respectively, suggesting the long-term electrolysis in alkaline media induced the formation of CoO in the surface layer (Fig. 5c). XRD pattern of such post-electrolysis sample shows the dominant peaks of CoP (JCPDS: 29-0497) as well as several additional peaks assigned to CoO (JCPDS: 48-1719), indicating the bulk crystal structure of the B-CoP was preserved during the 20-h test (Fig. 5d). These observations indicate that the surface oxidation has no significant influence on the crystal structure of cobalt phosphide [19,41]. Furthermore, the surface oxidation was revealed by the XPS analysis (Fig. 5e-h). The O content is increased from 31% to 47% after long-term electrolysis, presumably because of formation of cobalt oxide species when exposure to strong

alkaline electrolyte. In the high-resolution XPS spectra of Co 2p, the peaks associated with the cobalt phosphides decrease sharply while the peaks corresponding to cobalt oxides increase after long-term electrolysis. Meanwhile, both P 2p and B 1s spectra suggests the increase in P-O/B-O peaks compared with P-O/B-O peaks, indicating the outmost cobalt oxide layer inhibits deeper oxidation of phosphide and CoP dominates the composition of the surface. Taken together, we can conclude that the good electrocatalytic activity of B-CoP originates from the B-doping regulated electronic structure in cobalt phosphide.

## 4. Conclusions

In summary, cobalt phosphide nanowire arrays with confined-doping of boron in the surface layer (B-CoP) has been synthesized by a facile redox reaction. Benefiting from B-doping in the surface layer of CoP, the B-CoP catalyst possesses enlarged ECSA, improved electric conductivity, and exhibits outstanding HER activity with largely decreased overpotential of 57 mV to achieve current density of  $100 \text{ mA cm}^{-2}$  than undoped CoP. Both experimental results and DFT calculations confirmed that B-doping caused the accumulation of more electrons around Co to form low-valence Co centers, and therefore regulated the electron structure in the surface layer of CoP with optimized  $\Delta G_{H^*}$  and accelerated reaction kinetics for HER. This work provides a versatile strategy for the design of efficient TMPs-based HER electrocatalysts with regulated electronic structure, which may be extended to the optimization of surface chemistry for other catalysts.

### CRedit authorship contribution statement

**Yingying Gao:** Investigation, Methodology, Validation, Data curation. **Sheng Qian:** Data curation, Software, Validation, Project administration. **Haijiao Wang:** Methodology, Data curation. **Wenzhi Yuan:** Methodology, Data curation. **Yu Fan:** Investigation, Validation. **Ningyan Cheng:** Data curation, Characterization. **Huaguo Xue:** Supervision, Resources. **Tengfei Jiang:** Funding acquisition, Project administration. **Jingqi Tian:** Conceptualization, Funding acquisition, Project administration, Resources, Writing – original draft & editing.



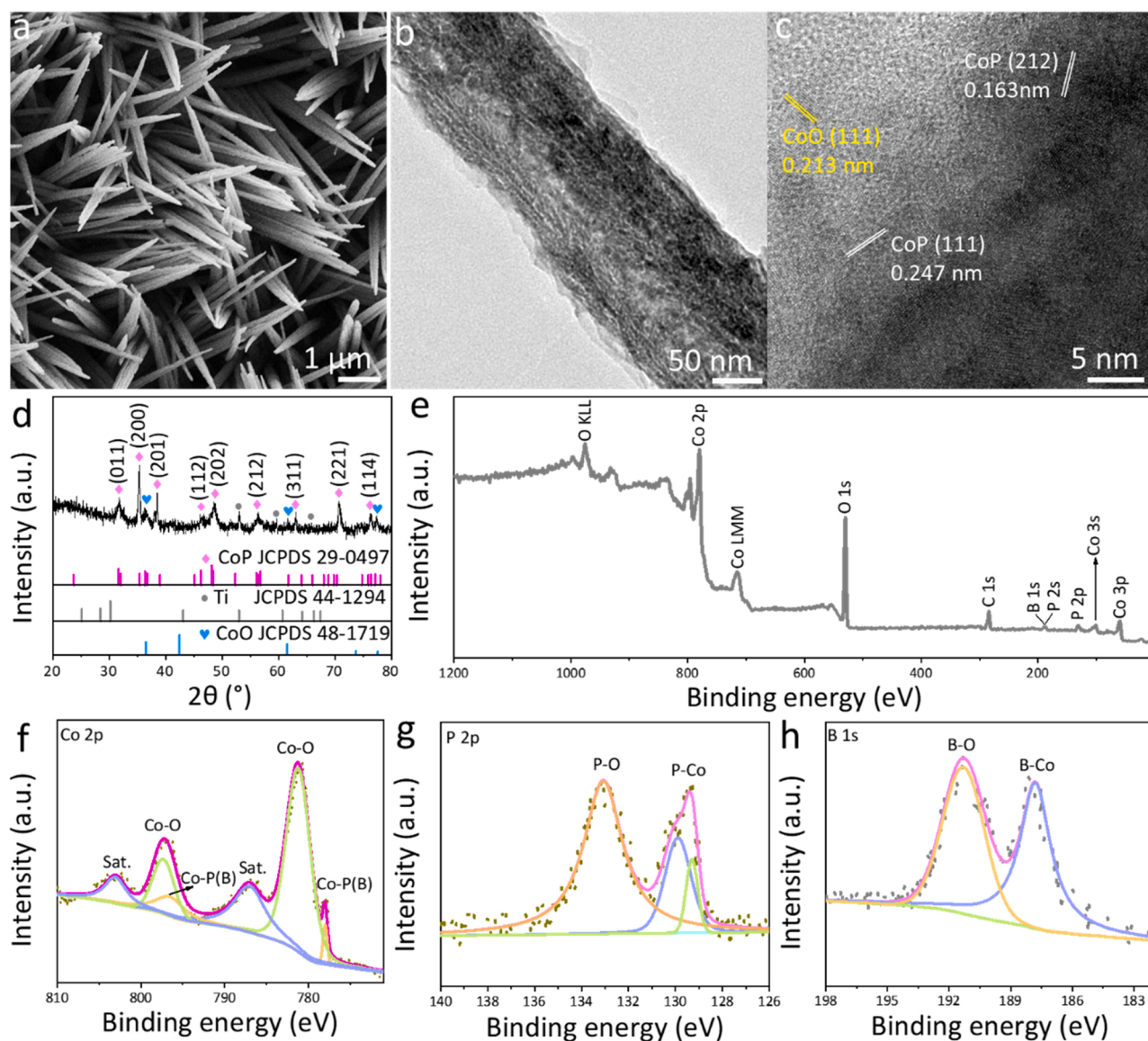


**Fig. 5.** The characterization of B-CoP after 20 h-electrolysis. (a) SEM, (b) TEM, (c) HRTEM image and (d) XRD pattern; (e) XPS survey spectrum, and high-resolution XPS spectrum of (f) Co 2p, (g) P 2p and (h) B 1s.

## Declaration of Competing Interest

The authors declare that they have no known competing financial interests or personal relationships that could have appeared to influence the work reported in this paper.

## Data availability

No data was used for the research described in the article.

## Acknowledgments

This work was financed by the National Natural Science Foundation of China (Grant No. 22102140), the Natural Science Foundation of Jiangsu Province (Grant No. BK20211602), the Six Talent Peaks Project in Jiangsu Province (2019-XCL-101), and the Specially-Appointed Professor Plan in Jiangsu Province.

## Appendix A. Supporting information

Supplementary data associated with this article can be found in the online version at [doi:10.1016/j.apcatb.2022.122014](https://doi.org/10.1016/j.apcatb.2022.122014).

## References

- [1] A. Han, X. Zhou, X. Wang, S. Liu, Q. Xiong, Q. Zhang, L. Gu, Z. Zhuang, W. Zhang, F. Li, D. Wang, L. Li, Y. Li, Nat. Commun. 12 (2021) 1–10.
- [2] R. Kukobat, M. Sakai, H. Tanaka, H. Otsuka, F. Vallejos-Burgos, C. Lastoskie, M. Masahiko, S. Yukichi, Y. Kaname, H. Takuya, K. Katsumi, Sci. Adv. 8 (2022) 3521.
- [3] I. Roger, M.A. Shipman, M.D. Symes, Nat. Rev. Chem. 1 (2017) 0003.
- [4] C. Hu, L. Zhang, J. Gong, Energy Environ. Sci. 12 (2019) 2620.
- [5] X. Long, G. Li, Z. Wang, H. Zhu, T. Zhang, S. Xiao, W. Guo, S. Yang, J. Am. Chem. Soc. 137 (2015) 11900–11903.
- [6] Y. Li, Z. Dong, L. Jiao, Adv. Energy Mater. 10 (2020), 1902104.
- [7] D.H. Song, D. Hong, Y. Kwon, H. Kim, J. Shin, H. Lee, E. Cho, J. Mater. Chem. A 8 (2020) 12069–12079.
- [8] X. Li, J. Wang, Adv. Mater. Interfaces 7 (2020), 2000676.
- [9] Y. Men, P. Li, J. Zhou, S. Chen, W. Luo, O.O. 1 (2020) 100136.
- [10] S. El-Refaei, P. Russo, N. Pinna, ACS Appl. Mater. Interfaces 13 (2021) 22077–22097.
- [11] Y. Men, P. Li, J. Zhou, G. Cheng, S. Chen, W. Luo, ACS Catal. 9 (2019) 3744–3752.

- [13] W. Kwong, E. Gracia-Espino, C. Lee, R. Sandström, T. Wågberg, J. Messinger, *ChemSusChem* 10 (2017) 4544–4551.
- [14] Y. Gao, Q. Wang, T. He, J. Zhang, H. Sun, B. Zhao, B. Xia, Y. Yan, Y. Chen, *Chem. Front.* 6 (2019) 2686–2695.
- [15] F. Hu, S. Zhu, S. Chen, Y. Li, L. Ma, T. Wu, Y. Xiong, *Adv. Mater.* 29 (2017), 1606570.
- [16] B. Zhang, J. Shan, W. Wang, P. Tsiakaras, Y. Li, *Small* 18 (2022), 2106012.
- [17] S. Li, L. Wang, H. Su, A. Hong, Y. Wang, H. Yang, L. Ge, W. Song, J. Liu, T. Ma, X. Bu, P. Feng, *Adv. Funct. Mater.* 32 (2022), 2200733.
- [18] G. Zhou, M. Li, Y. Li, H. Dong, D. Sun, X. Liu, L. Xu, Z. Tian, Y. Tang, *Adv. Funct. Mater.* 30 (2020), 1905252.
- [19] R. Xu, T. Jiang, Z. Fu, N. Cheng, X. Zhang, K. Zhu, H. Xue, W. Wang, J. Tian, P. Chen, *Nano Energy* 78 (2020), 105347.
- [20] Q. Zhou, Z. Shen, C. Zhu, J. Li, Z. Ding, P. Wang, F. Pan, Z. Zhang, H. Ma, S. Wang, H. Zhang, *Adv. Mater.* 30 (2018), 1800140.
- [21] J. Zhuo, M. Caban-Acevedo, H. Liang, L. Samad, Q. Ding, Y. Fu, M. Li, *ACS Catal.* 5 (2015) 6355–6361.
- [22] S. Shen, Z. Wang, Z. Lin, K. Song, Q. Zhang, F. Meng, L. Gu, W. Zhong, *Adv. Mater.* 34 (2022), 2110631.
- [23] E. Cao, Z. Chen, H. Wu, P. Yu, Y. Wang, F. Xiao, S. Chen, S. Du, Y. Xie, Y. Wu, Z. Ren, *Angew. Chem. Int. Ed.* 59 (2020) 4154–4160.
- [24] J. Perdew, K. Burke, M. Ernzerhof, *Phys. Rev. Lett.* 77 (1995) 3865.
- [25] G. Kresse, D. Joubert, *Phys. Rev. B* 59 (1999) 1758.
- [26] D. Chadi, *Phys. Rev. B* 16 (1977) 5188–5192.
- [27] L. Gong, D. Zhang, C. Lin, Y. Zhu, Y. Shen, J. Zhang, X. Han, L. Zhang, Z. Xia, *Adv. Energy Mater.* 9 (2019), 1902625.
- [28] J. Nørskov, T. Bligaard, A. Logadottir, J. Kitchin, J. Chen, S. Pandalov, U. Stimming, *J. Electrochem. Soc.* 5 (2005), 12154–12154.
- [29] J. Nørskov, J. Rossmeisl, A. Logadottir, L. Lindqvist, J. Kitchin, T. Bligaard, H. Jónsson, *J. Chem. Phys. B* 108 (2004) 17886–17892.
- [30] L. Bendavid, E. Carter, *J. Phys. Chem. C* 117 (2013) 26048–26059.
- [31] T. Chen, X. Li, C. Qiu, W. Zhu, H. Ma, S. Chen, O. Meng, *Biosens. Bioelectron.* 53 (2014) 200–206.
- [32] J. Tian, Q. Liu, A. Asiri, X. Sun, *J. Am. Chem. Soc.* 136 (2014) 7587–7590.
- [33] C. Tang, R. Zhang, W. Lu, L. He, X. Jiang, A. Asiri, X. Sun, *Adv. Mater.* 29 (2017), 1602441.
- [34] R. Zhang, X. Wang, S. Yu, T. Wen, X. Zhu, F. Yang, X. Sun, X. Wang, W. Hu, *Adv. Mater.* 29 (2017), 1605502.
- [35] M. Liu, Q. He, S. Huang, W. Zou, J. Cong, X. Xiao, P. Li, J. Cai, L. Hou, *ACS Appl. Mater. Interfaces* 13 (2021) 9932–9941.
- [36] Y. Zhao, J. Zhang, Y. Xie, B. Sun, J. Jiang, W. Jiang, S. Xi, H. Yang, K. Yan, S. Wang, X. Guo, P. Li, Z. Han, X. Lu, H. Liu, G. Wang, *Nano Lett.* 21 (2021) 823–832.
- [37] P. Zhou, Q. Zhang, Z. Xu, Q. Shang, L. Wang, Y. Chao, S. Guo, *Adv. Mater.* 32 (2020), 1904249.
- [38] Y. Xu, R. Wang, J. Wang, Y. Zhang, T. Jiao, *J. Energy Chem.* 71 (2022) 36–44.
- [39] Q. Yang, B. Zhu, F. Wang, C. Zhang, J. Cai, P. Jin, L. Feng, *Nano Res.* 15 (2022) 5134–51421.
- [40] J. Xie, Z. Liu, J. Li, L. Feng, M. Yang, Y. Ma, D. Liu, L. Wang, Y. Chai, B. Dong, *J. Energy Chem.* 48 (2022) 328–333.
- [41] Y. Zhang, L. Gao, E.J.M. Hensen, J.P. Hofmann, *ACS Energy Lett.* 3 (2018) 1360–1365.